Vector treatment of second-harmonic generation produced by tightly focused vignetted Gaussian beams

Ara A. Asatryan,* Colin J. R. Sheppard,† and C. Martijn de Sterke

School of Physics, University of Sydney, New South Wales 2006, Australia

Received January 21, 2004; revised manuscript received June 24, 2004; accepted July 20, 2004

We present a fast and accurate method to calculate the vector-field distribution of a focused Gaussian beam. This method is applied to calculate the second harmonic that is generated by such a beam from a sample in the undepleted pump approximation. These calculations can be used to model second-harmonic imaging in an optical microscope with a wide aperture. © 2004 Optical Society of America

OCIS codes: 260.1960, 180.2520, 190.4350.

1. INTRODUCTION

Nonlinear microscopy originated in the 1970s from the work of Hellwarth and Christensen.[1] Subsequently, Gannaway and Sheppard[2] reported the production of microscope images from crystals, using scanning and second-harmonic generation with a focused laser beam. Sheppard and Kompfner[3] pointed out that the high magnitudes of electric field produced at the focus of a focused laser beam would be expected to result in the excitation of a range of different nonlinear optical effects other than second-harmonic generation, including the generation of sum frequencies, Raman scattering, and two-photon fluorescence. They described how the efficiency of generation is improved by short pulses. Widespread use of nonlinear microscopy therefore awaited the availability of commercial ultrashort laser sources. Although two-photon fluorescence microscopy is now a well-established technique in biological studies, the use of harmonic generation in biological applications is still comparatively in its infancy. Important applications are the enhancement of contrast in unlabeled biological material,[4–6] imaging of cell membranes[7,8] and membrane potentials,[9,10] and imaging of surfaces[11] and thin films.[12]

The theory of second-harmonic generation by weakly focused Gaussian beams is well known.[13] An important property is that the Gouy phase shift experienced on traversing the focus limits the thickness of a medium that can efficiently generate second-harmonic radiation. However, this theory assumes that the angular spectrum of the incident radiation effectively propagates all at the same angle relative to the material axes. Thus phase matching can be achieved for the complete angular spectrum. This assumption is obviously not valid when using a microscope objective of high numerical aperture. Second-harmonic generation is also a vector effect, and it is known that the polarization of a tightly focused laser beam varies throughout the focal region, including both a cross component and an axial component of polarization for illumination with a plane-polarized beam. In spite of its importance, the vector theory of the multiple-photon imaging has not been addressed so far.

Our aim here is to develop a general method that can effectively calculate the nonlinear multiphoton imaging generated by a tightly focused vignetted Gaussian beam. Although the method is applied to second-harmonic imaging by a focused vector Gaussian beam, it can straightforwardly be extended to include other types of nonlinearities. The structure of the paper follows. In Section 2, we first present a method for accurate and fast calculation of a wave field of the vector focused Gaussian beam, while in Section 3 we investigate the properties of the second-harmonic generation produced by a beam. Finally, in Section 4 we discuss our results and conclude.

2. WAVE FIELD OF FOCUSED, VECTOR GAUSSIAN BEAMS

Here we present an efficient and accurate method for calculating the vector field in the focal region of a Gaussian beam. There are a number of ways in which this can be achieved. In the scalar approximation, the wave field at the focus of a lens of large Fresnel number can be described by the Debye integral.[14] More rigorous descriptions that include the evanescent waves are given by the Kirchoff and Rayleigh–Sommerfeld integrals.[15] The Debye representation was extended to take into account the vector nature of the electromagnetic waves by Ignatovsky[16] and by Richards and Wolf.[17] This extension gives accurate account of the intensity distribution in the focal region for many practical applications. Yoshida and Asakura used this extension to calculate the electromagnetic field of a focused vignetted Gaussian beam.[18] In the vector Debye approximation[14] for a linearly polarized wave along the x axis, the components of the electric field $\mathbf{E}$ at the focus can be written as

$$E_x = -\frac{iA}{\pi}\int_0^{\alpha}\int_0^{2\pi} B(\theta,\ \phi)\sqrt{\cos\theta}\sin\theta \times [\cos\theta + (1 - \cos\theta)\sin^2\phi]\exp(ik_s\cdot\mathbf{r}_P)\mathrm{d}\theta\mathrm{d}\phi, \tag{1}$$

$$E_y = \frac{iA}{\pi}\int_0^{\alpha}\int_0^{2\pi} B(\theta,\ \phi)\sqrt{\cos\theta}\sin\theta \times (1 - \cos\theta)\cos\phi\sin\phi\exp(ik_s\cdot\mathbf{r}_P)\mathrm{d}\theta\mathrm{d}\phi, \tag{2}$$

$$E_z = \frac{iA}{\pi}\int_0^{\alpha}\int_0^{2\pi} B(\theta,\ \phi)\sqrt{\cos\theta}\sin^2\theta\cos\phi \times \exp(ik_s\cdot\mathbf{r}_P)\mathrm{d}\theta\mathrm{d}\phi, \tag{3}$$

where $A = kf/2$. Here $\mathbf{r}_P$ is the radius vector of the observation point measured from the focal spot, f is the focal length, $k = 2\pi/\lambda$ is the wave number, $B(\theta,\ \phi)$ is the distribution of the amplitude of the incident wave on the aperture of the lens, $\tan\alpha = a/f$ is the half of the angular aperture seen from the focus, and a is the radius of the aperture. Here the direction of the propagation is along the z axis. In this paper, we consider only azimuthally symmetric distributions, for which amplitude factor B does not depend on the azimuthal angle ϕ. The unit vector $\mathbf{s}$ determines the direction of the propagation of the virtual rays originated at the surface of the lens. For a Gaussian beam, $B(\theta,\ \phi)$ is given by

$$B(\theta,\ \phi) = \exp(-f^2\tan^2\theta/W^2), \tag{4}$$

where W is the width. For an incident plane wave, where $B(\theta,\ \phi) = 1$, the integrals (1)–(3) have been calculated in the form of a series that involve Gegenbauer ultraspherical polynomials and spherical Bessel functions by Kant.[19] Sheppard and Török[20] noted that Gegenbauer polynomials are closely related to the associated Legendre functions P_l^m and suggested that Kant's expansion perhaps could be interpreted in terms of multipole fields. In contrast to Sheppard and Török,[20] who use multipoles to find the field at the focal points, here we used the multipole expansions to calculate the diffraction integrals efficiently. Below, we explicitly show how this connection can be established.

First, we expand the plane wave $\exp(ik\mathbf{s}\cdot\mathbf{r}_P)$, where $k_s = k\mathbf{s}$ in Eqs. (1)–(3) in the series[21]

$$\exp(ik\mathbf{s}\cdot\mathbf{r}_P) = 4\pi\sum_{l=0}^{\infty} i^l j_l(kr_P) \times \sum_{m=-l}^{l} Y_{lm}^*(\theta,\ \phi)Y_{lm}(\theta_P,\ \phi_P), \tag{5}$$

where the Y_{lm} are the spherical harmonics defined as in Jackson,[21] while θ_P and ϕ_P are the spherical angles of the observation point $\mathbf{r_P}$. After substitution of Eq. (5) into Eqs. (1)–(3) and integration over the azimuthal angle ϕ, the components of the electric field $\mathbf{E}$ can be written as an absolutely convergent series by the properties of the spherical Bessel functions,[22] as

$$E_x = 4\pi\sum_{l=0}^{\infty} I_l^{(0)} i^l j_l(kr_P)Y_{l,0}^*(\theta_P,\ \phi_P) + 4\pi\sum_{l=2}^{\infty} I_l^{(2)} i^l j_l(kr_P) \times \frac{[Y_{l,2}(\theta_P,\ \phi_P) + Y_{l,2}^*(\theta_P,\ \phi_P)]}{2}, \tag{6}$$

$$E_y = 4\pi\sum_{l=2}^{\infty} I_l^{(2)} i^l j_l(kr_P)\frac{[Y_{l,2}(\theta_P,\ \phi_P) - Y_{l,2}^*(\theta_P,\ \phi_P)]}{2i}, \tag{7}$$

$$E_z = 4\pi\sum_{l=1}^{\infty} I_l^{(1)} i^l j_l(kr_P)\frac{[Y_{l,1}(\theta_P,\ \phi_P) + Y_{l,1}^*(\theta_P,\ \phi_P)]}{2}, \tag{8}$$

where the integrals $I_l^{(0)}$, $I_l^{(1)}$, and $I_l^{(2)}$ are given by

$$I_l^{(0)} = -\frac{iA}{\pi}\sqrt{\frac{\pi(2l+1)}{4}}\int_{\cos\alpha}^{1} B(x)\sqrt{x}(1+x)P_l^{(0)}(x)\mathrm{d}x, \tag{9}$$

$$I_l^{(2)} = \frac{iA}{\pi}\sqrt{\frac{\pi(2l+1)}{4}\frac{(l-2)!}{(l+2)!}}\int_{\cos\alpha}^{1} B(x)\sqrt{x}(1-x) \times P_l^{(2)}(x)\mathrm{d}x, \tag{10}$$

$$I_l^{(1)} = \frac{iA}{\pi}\sqrt{\frac{\pi(2l+1)}{l(l+1)}}\int_{\cos\alpha}^{1} B(x)\sqrt{x(1-x^2)}P_l^{(1)}(x)\mathrm{d}x, \tag{11}$$

where $P_l^{(1)}(x)$ represents generalized Legendre polynomials. For the incident Gaussian beam (4), the amplitude distribution B takes the form

$$B(x) = \exp[-f^2(1 - x^2)/(W^2x^2)]. \tag{12}$$

To calculate field, the series (6)–(8) must be truncated at some value $l = l_{\max}$, where $l_{\max}$ is determined by

$$l_{\max} \geq kr_P. \tag{13}$$

In most applications, including that of interest here, one is interested in the distribution of the wave field in the focal region. When evaluating the field using the series (6)–(8), we require approximately kr_P terms, where r_P is the distance from the focal point. Since the region of interest here extends several wavelengths out from the focal point, $kr_P \geq 10$–20, and we have found that 30 terms gives sufficient precision for each field point. In contrast, for the direct evaluation of (1)–(3), the integrands of which are strongly oscillatory, we require a two-dimensional integration through the entire focal region. Since we require roughly 20 integration points per wavelengths for accurate evaluation, the two-dimensional integral requires approximately $100 \times 100 = 10^4$ function evaluations. Therefore the evaluation via the absolutely convergent series (6)–(8) is much more efficient.

The integrals $I_l^{(0)} - I_l^{(2)}$ in Eqs. (9)–(11) can be calculated numerically. They are oscillating functions of l, and some difficulties can be associated with their calculation for large values of l ($l \geq 30$). However, this is never a significant issue, because in most applications

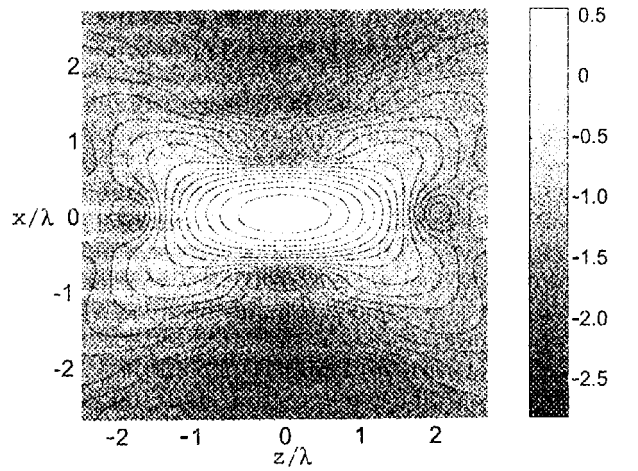

Fig. 1. Intensity distribution in the xz plane near the focus of a convergent Gaussian beam. The initial Gaussian beam is taken to be linearly polarized along the x axis.

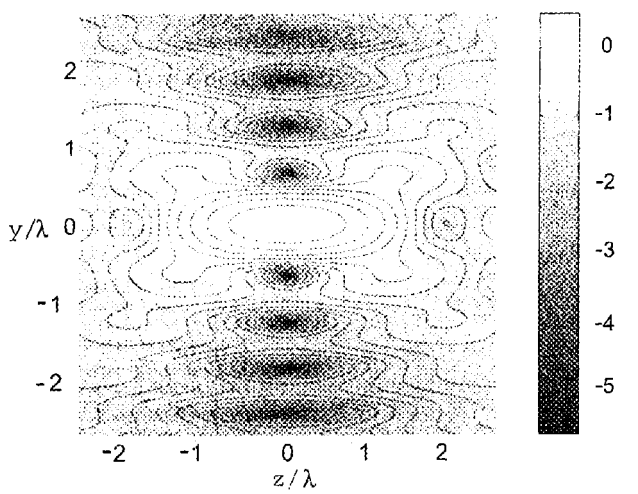

Fig. 2. As in Fig. 1, but in the yz plane.

only the field in the vicinity of the focus is needed, where condition (13) holds. Note that the main advantage of Eqs. (6)–(8) over the direct integration of Eqs. (1)–(3)[17,18] is that it is not necessary to calculate highly oscillating integrals like Eqs. (1)–(3) for every observation point. So once the amplitudes of the multipoles $I_j^{(i)}$ are calculated, the field distribution at the focus can be determined by the summation of the absolutely convergent series (6)–(8). Thus the method is highly accurate and numerically effective.

As an example, we consider an incoming vector Gaussian beam that is linearly polarized in the x direction and that is focused by a lens of focal length f and aperture radius a that is positioned at the beam waist, which has a radius W. The lens has a numerical aperture $\sin\alpha = a/\sqrt{a^2 + f^2} = 0.5$, and we choose W such that the vignetting of the intensity level of the Gaussian beam at the edge of the aperture is $\exp(-2a^2/W^2) = 0.7$, so that $W/a \approx 2.38$. Finally, we take $f/\lambda = 577$. These are the typical parameters used in a nonlinear microscope. In Figs. 1–3, we plot the logarithm of the intensity distributions $\log_{10}(\mathbf{E}\mathbf{E}^*)$ of the field in the vicinity of the focus for the xz, yz, and xy main sections. The intensity distribution is symmetric with respect to the focal plane (see Figs. 1 and 2), which is a consequence of the Debye approximation. The typical Airy rings of the intensity distribution are clearly seen in the focal plane ($z = 0$) in Fig. 3. Note that the field intensity is mostly concentrated near the focal region. In Fig. 4, we plot the intensity distribution $|E|^2$ along x and y axes at the focal plane $z = 0$. The intensity along the x axis, the polarization direction of the incident wave, is slightly wider than along the y axis. In Fig. 5 we plot the same dependence, but along the z axis. Note that in actual units, rather than the dimensionless units used in Figs. 4 and 5, the wave-field distribution along the optical z axis is much wider than that in the transverse direction.

3. SECOND-HARMONIC GENERATION BY A FOCUSED VECTOR GAUSSIAN BEAM

In this section, we calculate the second-harmonic generation by the focused Gaussian beam considered in the pre-

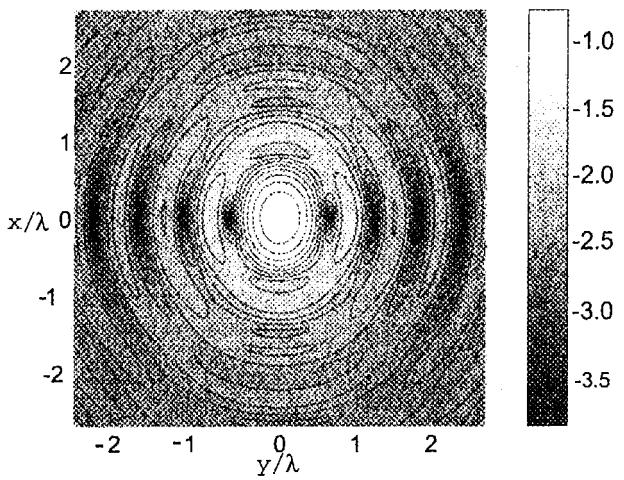

Fig. 3. As in Fig. 1, but in the xy plane. The Airy pattern is clearly seen.

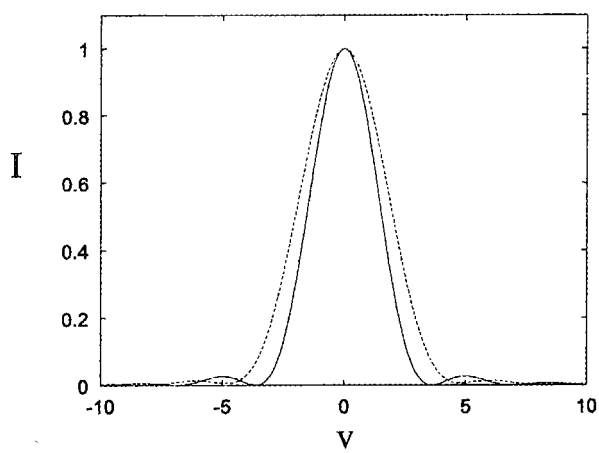

Fig. 4. Intensity distribution $I = |E|^2$ along x (dashed curve) and y axes (solid curve) in the focal plane $z = 0$. We use the optical coordinate scale $v = k\sqrt{x^2 + y^2}\sin\alpha$, and we normalize the intensity with respect to the value at the focus.

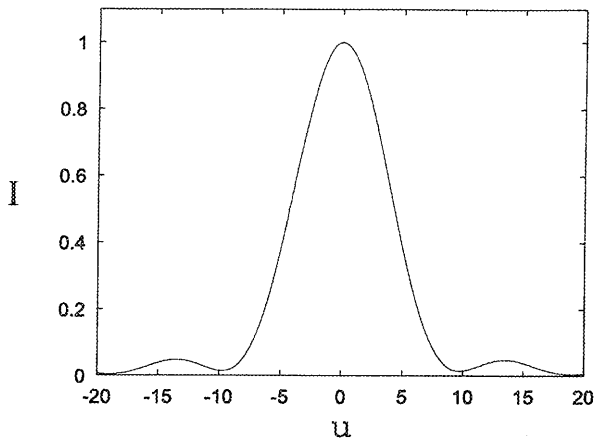

Fig. 5. Intensity distribution $I = |E|^2$ along the optical z axis. We used optical coordinate scale $u = kz \sin^2 \alpha$, and we normalize the intensity with respect to the value at the focus.

vious section in Eqs. (6)–(8). The electric field E_n of the nth harmonic in the undepleted pump approximation satisfies the equation[23]

$$\nabla \times \nabla \times \mathbf{E}_n - \frac{\omega_n^2}{c^2}\epsilon^{(1)}(\omega_n)\mathbf{E}_n = \frac{4\pi\omega_n^2}{c^2}\mathbf{P}_n^{(\mathrm{NL})}(\mathbf{r}). \tag{14}$$

Here E_n is the amplitude of the nth harmonic, $\epsilon^{(1)}(\omega_n)$ is the linear part of the dielectric constant of the medium, which we considered here to be isotropic and dispersive, and $\mathbf{P}_n^{(\mathrm{NL})}(\mathbf{r})$ is the nonlinear part of the polarization tensor. From Eq. (14), the amplitude of the electric field for the second harmonic $E_2(\omega_2 = 2\omega)$ can be written as

$$\nabla \times \nabla \times \mathbf{E}_2 - k_2{}^2\mathbf{E}_2 = \frac{16\pi k^2}{\epsilon^{(1)}(\omega)}\mathbf{P}_2^{(\mathrm{NL})}(\mathbf{r}), \tag{15}$$

where $k_2 = 2\omega\sqrt{\epsilon^{(1)}(\omega_2)}/c$ is the wave number of the second harmonic, and $k = \omega\sqrt{\epsilon^{(1)}(\omega)}/c$ is the wave number of the focused Gaussian beam, while $\mathbf{P}_2^{(\mathrm{NL})}(\mathbf{r})$ is the nonlinear polarization of the second harmonic given by

$$P_{2i}(\omega_2) = \chi_{ijk}^{(2)}(\omega_2;\ \omega,\ \omega)E_j(\omega)E_k(\omega), \tag{16}$$

with a summation over repetitive indices.

The formal solution of Eq. (15) can be written as

$$\mathbf{E}_2 = \frac{16\pi k^2}{\epsilon^{(1)}(\omega)}\int_{V'}\bar{\mathbf{G}}(\mathbf{r};\ \mathbf{r}')\cdot\mathbf{P}_2^{(\mathrm{NL})}(\mathbf{r}')\mathrm{d}V', \tag{17}$$

where $\bar{\mathbf{G}}(\mathbf{r};\ \mathbf{r}')$ is the free space Green tensor,[24] given by

$$\bar{G}(\mathbf{r};\ \mathbf{r}') = \left(\mathbf{I} + \frac{1}{k_2{}^2}\nabla\nabla\right)\frac{\exp(ik_2|\mathbf{r} - \mathbf{r}'|)}{4\pi|\mathbf{r} - \mathbf{r}'|}, \tag{18}$$

where $\mathbf{I}$ is the unit tensor.

As mentioned in Section 1, the field is mostly concentrated at the focal spot. This region therefore contributes mostly to the second-harmonic generation from Eq. (16). Thus for a nonlinear medium of large extent, we can restrict the region of the integration in Eq. (17) to the neighborhood of the focus. In fact, for the numerical integration V', we choose here a prism around the focus, while the use of a spherical integration volume is discussed in Section 4.

For simplicity, we take the dielectric constant of the sample to be unity $\epsilon^{(1)}(\omega)$; thus we disregard the Fresnel reflection of the converging Gaussian beam at the surface of the sample. However, we can take into account the effects of the dispersion and investigate the consequences of phase matching $k_2 = 2k$, when $\epsilon^{(1)}(\omega_2) = \epsilon^{(1)}(\omega)$, and phase mismatching, when $\epsilon^{(1)}(\omega_2) \neq \epsilon^{(1)}(\omega)$, but we use the former only.

Below, we take $\chi^{(2)}$ to be real, although our method also applies to complex $\chi^{(2)}$. There are various symmetry relations between the different components of $\chi_{ijk}^{(2)}$.[23] Because the components of the tensor $\chi^{(2)}$ for most biological tissues are not well known, and vary spatially in any case, as an example, we consider the second-harmonic produced by $BaTiO_3$ crystals. This crystal belongs to the group of crystals with tetragonal C_{4v} point symmetry. The largest elements of the nonlinear susceptibility tensor are[23]

$$\begin{aligned}\chi_{131}^{(2)} &= \chi_{113}^{(2)} = \chi_{232}^{(2)} = \chi_{223}^{(2)} = -82,\\ \chi_{311}^{(2)} &= \chi_{322}^{(2)} = -86,\\ \chi_{333}^{(2)} &= -16,\end{aligned} \tag{19}$$

in 10^{-9} esu. To find the values of $\chi^{(2)}$ tensor in SI system of units, its components need to be multiplied by $4\pi/(3 \times 10^4) = 4.189 \times 10^{-4}$ to obtain $\chi^{(2)}$ in units of m/V.[23]

We calculate the intensity distribution of the second-harmonic generation produced by the focused Gaussian beam discussed in Section 2. The orientation of the crystal with respect to the optical axis of the system is as follows: $x\|3$, $y\|1$, $z\|2$. The optical axis of the system is parallel to the z axis, and the incident field is linearly polarized along the x axis. The numerical integrations in Eq. (17) are carried out over the rectangular prism with the sides $x/\lambda = [-2{:}2]$, $y/\lambda = [-2{:}2]$, and $z/\lambda = [-3{:}3]$. This region corresponds to the maximum intensity at the focus, and hence only this part of the sample contributes substantially to the generation of the

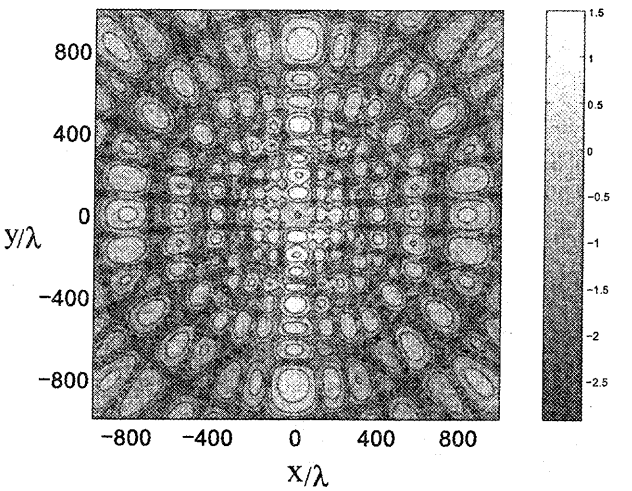

Fig. 6. Distribution of $\log_{10}|E_{x2}|^2$ in the xy plane at $z/\lambda = 577$ from the focus. The coordinates x and y are measured in terms of the wavelength.

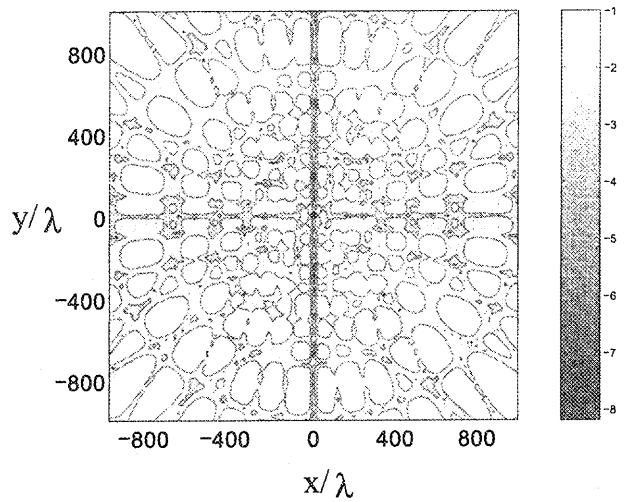

Fig. 7. As in Fig. 6, but for $\log_{10}|E_{y2}|^2$ component of the second harmonic.

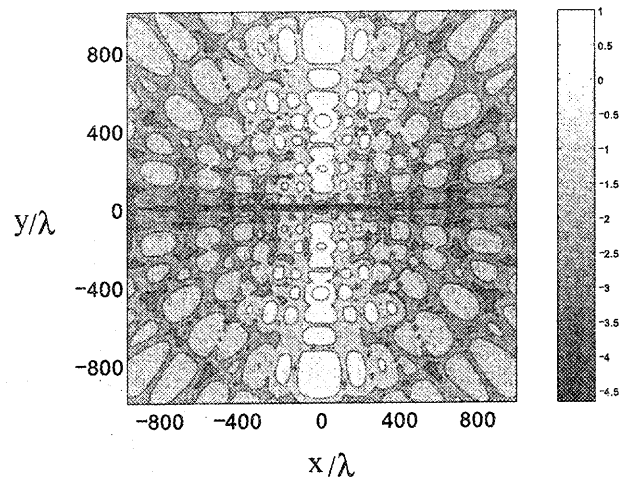

Fig. 8. As in Fig. 6, but for $\log_{10}|E_{z2}|^2$ component of the second harmonic.

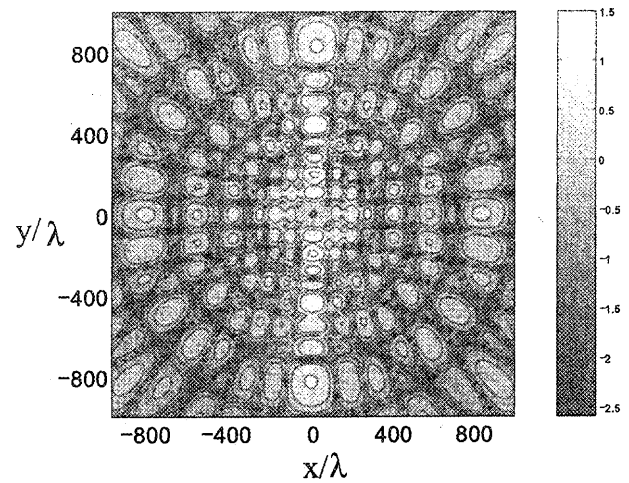

Fig. 9. Intensity distribution $\log_{10}|E_2|^2$ of the second harmonic in the xy plane.

second harmonic. We consider the case in which the phase-matching condition holds ($k_2 = 2k$), and we calculate the intensity distribution in the plane $z/\lambda = 577$, which is one focal length away from the focus.

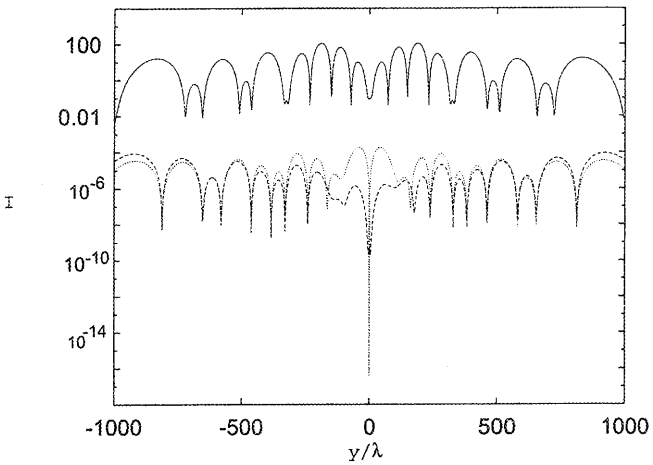

Fig. 10. Section of Figs. 6–8 versus y/λ for $|E_{x2}|^2$ (solid curve), for $|E_{y2}|^2$ (dotted curve), and for $|E_{z2}|^2$ (dashed curve).

In Figs. 6–9, we plot the distribution of the field components of the generated second harmonic $|E_{x2}|^2$, $|E_{y2}|^2$, $|E_{z2}|^2$, while Fig. 10 shows the total intensity distribution $|E_2|^2$. In this way, we present the data in a form that is easily compared with experiment.[7] For this orientation of the crystal and incident field, we observe that the various components of the second-harmonic field satisfy $|E_{y2}| \leqslant |E_{z2}| < |E_{x2}|$. Hence the dominant contribution comes from the E_{x2} component, even though it is generated via the smallest of the quadratically nonlinear tensor elements $\chi^{(2)}_{333}$ [see Eq. (20)]. This is seen in Fig. 10, where we plot the section of Figs. 6–9 along the y axis. The second-harmonic field decreases at the points closer to the optical axes z axis (see Fig. 10).

4. DISCUSSION AND CONCLUSIONS

The contribution to the second harmonic is dominated by the E_x component of the field, which is also the polarization direction of the incoming fundamental field. The relevant element of the nonlinear susceptibility is $\chi^{(2)}_{333}$, which is more than a factor of 5 smaller than the other nonzero tensor elements [see Eqs. (20)]. This is also the only contribution that arises in the scalar approximation to the electric fields. However, in the vector treatment given here, the second harmonic is generated in all field components. The y components are generated by the xyy component of the $\chi^{(2)}$ tensor. This contribution is expected to be small since it relies on the minor y-polarized component of the incoming fundamental field. In addition, the contributions from the two positions (x, y, z) and $(-x, -y, z)$ are π out of phase and thus cancel on the z axis, as seen in Fig. 7. Thus, even though the relevant $\chi^{(2)}$ element is more than a factor of 5 larger than that used for generating the x-polarized second harmonic, the y-polarized second-harmonic field is very small compared with that polarized in the x direction. The z component of the second-harmonic field is due to the xzz and zxz elements of $\chi^{(2)}$, and it relies not only on a minor field component of the fundamental field, but also on a minor component of the second-harmonic field. The latter can be

understood intuitively by the observation that the xzz and zxz elements generate dipoles that point in the z direction and oscillate at the second-harmonic frequency. Clearly the coupling of this radiation into a wave propagating in the z direction is inefficient.

We thus find that, even though the scalar-allowed second-harmonic generation process makes use of a small $\chi^{(2)}$ tensor element, it nonetheless leads to the largest contribution to the second-harmonic intensity. The y-polarized minor second-harmonic component may be detected behind a high-quality polarizer. The information that is obtained would be complementary to that obtained using the major second-harmonic field component.

Even though we have taken the nonlinear optical medium here to be crystalline, nonlinear microscopy is usually applied to biological samples, which are unlikely to be crystalline. An analysis of such a system is more difficult than the present one, and we do not consider this case here. However, we note that the method developed here does apply to this case.

We have presented an effective and accurate method of calculation of the wave field of the vector focused Gaussian beam at the focal region and calculated the second-harmonic generation produced by this beam. The method is highly accurate and robust. It takes only 30 s to calculate plots as in Fig. 4 with 301×301 resolution on a personal computer with a 700-MHz processor. This speed allows us to carry out the integration in Eq. (17) with high accuracy and high resolution. The integration process in Eq. (17) can be further improved if one chooses the integration region in Eq. (17) as a sphere. Then it is possible to integrate the angular variables in Eq. (17) in closed form in terms of the Wigner $3-j$ coefficients and products of three spherical Bessel functions. The remaining radial part integration can then also be done in closed form for some values of the angular momentum. However, such calculations are outside the scope of this paper.

The method presented here is flexible and can be applied to calculate the field distribution from the reflection from a paraboloidal mirror, mixed dipole radiation, and others. Although we took the incident field to be linearly polarized, the method can be applied to arbitrary incident polarization, and the polarization of the resulting second-harmonic field can be presented in a number of ways. Here we have chosen to express it in terms of the components pointing in the x, y, and z directions determined by the propagation and polarization directions of the incoming field. Although we could have expressed them straightforwardly in terms of s and p components, it was pointed out by Moreaux that the present representation is most convenient when comparing with experiment.[7] Finally, the method can also be applied to nonuniform samples, or to samples with complex $\chi^{(2)}$ (Ref. 25), and to model nonlinear multiphoton imaging using third-[26] and higher-harmonic generation.

ACKNOWLEDGMENTS

This work was supported by the University of Sydney's Funding of Research Strengths Initiative. Helpful discussions with P. Lukins are acknowledged.

*Present address: School of Mathematical Sciences, University of Technology Sydney, New South Wales 2007, Australia.

†Present address: Department of Bioengineering, National University of Singapore, 9 Engineering Drive 1, Singapore 117576.

REFERENCES

1. R. Hellwarth and P. Christiansen, "Nonlinear optical microscope using second harmonic generation," Appl. Opt. **14**, 247–248 (1975).
2. J. N. Gannaway and C. J. R. Sheppard, "Second-harmonic imaging in the scanning optical microscope," Opt. Quantum Electron. **10**, 435 (1978).
3. C. J. R. Sheppard and R. Kompfner, "Resonant scanning optical microscope," Appl. Opt. **17**, 2879–2882 (1978).
4. I. Freund, M. Deutsch, and A. Sprecher, "Connective tissue polarity, optical second harmonic microscopy, crossed-beam summation and small-angle scattering in rat-tail tendon," Biophys. J. **50**, 693–712 (1986).
5. Y. Guo, P. P. Ho, A. Tirksliunas, F. Liu, and R. R. Alfano, "Optical harmonic generation from animal tissues by the use of picosecond and femtosecond laser pulses," Appl. Opt. **35**, 6810–6813 (1996).
6. G. Cox, E. Kable, A. Jones, I. Fraser, F. Manconi, and M. D. Gorrell, "3-dimensional imaging of collagen using second harmonic generation," J. Struct. Biol. **141**, 53–62 (2003).
7. L. Moreaux, O. Sandre, and J. Mertz, "Membrane imaging by second-harmonic generation microscopy," J. Opt. Soc. Am. B **17**, 1685–1694 (2000).
8. J. Mertz and L. Moreaux, "Multi-harmonic light microscopy: theory and applications to membrane imaging," in *Multiphoton Microscopy in the Biomedical Sciences*, A. M. Periasamy and P. T. C. So, eds., Proc. SPIE **4262**, 9–17 (2001).
9. G. Peleg, A. Lewis, M. Linial, and L. Loew, "Nonlinear optical measurement of membrane potential around single molecules at selected cellular sites," Proc. Natl. Acad. Sci. U.S.A. **96**, 6700–6704 (1999).
10. P. J. Campagnola, M. Wei, A. Lewis, and L. M. Loew, "High-resolution nonlinear optical imaging of live cells by second harmonic generation," Biophys. J. **77**, 3341–3349 (1999).
11. R. Gauderon, P. B. Lukins, and C. J. R. Sheppard, "Optimization of second harmonic generation microscopy," Micron **32**, 691–700 (2001).
12. J. Vydra and M. Eich, "Mapping of the lateral polar orientation distribution in second-order nonlinear thin films by scanning second-harmonic microscopy," Appl. Phys. Lett. **72**, 275–277 (1998).
13. G. D. Boyd and D. A. Kleinman, "Parametric interaction of focused Gaussian light beams," J. Appl. Phys. **39**, 3597–3639 (1968).
14. M. Born and E. Wolf, *Principles of Optics*, 6th ed. (Cambridge University, Cambridge, 1997).
15. L. Mandel and E. Wolf, *Optical Coherence and Quantum Optics* (Cambridge University, New York, 1995).
16. V. S. Ignatovsky, "Diffraction by a parabolic mirror having arbitrary opening," Trans. Opt. Inst. Petrograd **I**, paper IV (1920).
17. B. Richards and E. Wolf, "Electromagnetic diffraction in optical systems. II. Structure of the image field in an aplanatic system," Proc. R. Soc. London, Ser. A **253**, 358–379 (1959).
18. A. Yoshida and T. Asakura, "Electromagnetic field near the Focus of a Gaussian beam," Optik (Stuttgart) **41**, 281–292 (1974).
19. R. Kant, "An analytical solution of vector diffraction for focusing optical systems," J. Mol. Spectrosc. **40**, 337–347 (1993).
20. C. J. R. Sheppard and P. Török, "Efficient calculation of

electromagnetic diffraction in optical systems using a multipole expansion," J. Mod. Opt. **44**, 803–818 (1997).
21. J. D. Jackson, *Classical Electrodynamics* (Wiley, New York, 1998).
22. M. Abramowitz, *Handbook of Mathematical Functions* (Dover, New York, 1972).
23. R. W. Boyd, *Nonlinear Optics* (Academic, Boston, 1992).
24. W. C. Chew, *Waves and Fields in Inhomogeneous Media* (IEEE, New York, 1995).
25. P. A. Franken and J. F. Ward, "Optical harmonics and nonlinear phenomena," Rev. Mod. Phys. **35**, 23 (1963).
26. Ji-Xin Cheng and X. Sunney Xie, "Green's function formulation for third-harmonic generation microscopy," J. Opt. Soc. Am. B **19**, 1604–1610 (2002).